



Article

Chemical Synthesis of High-Stable Amorphous FeCo Nanoalloys with Good Magnetic Properties

Bai Yang *, Yue Wu, Xiaopan Li and Ronghai Yu

Key Laboratory of Aerospace Advanced Materials and Performance, Ministry of Education, School of Materials Science and Engineering, Beihang University, Beijing 100191, China; xspbcxhs@buaa.edu.cn (Y.W.); xiaopan-lee@buaa.edu.cn (X.L.); rhyu@buaa.edu.cn (R.Y.)

* Correspondence: byang@buaa.edu.cn; Tel./Fax: +86-10-8231-3786

Received: 19 January 2018; Accepted: 7 March 2018; Published: 9 March 2018

Abstract: It is difficult to fabricate high-purity amorphous FeCo alloys by traditional physical methods due to their weak glass forming ability. In this work, the fully amorphous FeCo nanoalloys with high purity and good stability have been prepared by a direct chemical reduction of Fe^{2+} and Co^{2+} ions with NaBH_4 as the reducing agent and polyvinylpyrrolidone (PVP) as the surfactant. The morphologies, surface compositions and particle sizes with their distribution of these amorphous samples can be effectively tuned by the suitable PVP additions. High crystallization temperature up to 468 °C, high saturation magnetization of $196.2 \text{ A} \cdot \text{m}^2 \cdot \text{kg}^{-1}$ and low coercivity of 83.3 Oe are obtained in amorphous FeCo nanoalloys due to their uniform distribution, weak surface oxidation and low surface B concentration. Good frequency-dependent magnetic properties can be also achieved in the fully compacted amorphous sample with a high density of 7.20 g/cm^3 . The simple chemical method, high stability and good magnetic properties for these amorphous FeCo nanoalloys promise their significant potential applications in high-power magnetic devices.

Keywords: amorphous FeCo nanoalloys; chemical reduction; good air stability; high thermal stability; good magnetic properties

1. Introduction

The nanosized FeCo or FeCo-based alloys have attracted much attention on their fabrication and characterization due to their good chemical properties and tunable magnetic properties varying with their compositions, which show a significant potential application in many technological areas such as numerous advanced magnetic devices, catalytic and medical applications [1–4]. In particular, compared with FeCo-based crystalline alloys, the amorphous counterparts have attracted more research interests for their combined good mechanical, electrical and magnetic properties including good deformability, high fracture strength, high resistivity and low coercivity, which make them a crucial soft magnetic material for high-power and high-frequency applications [5–8]. Commonly, these amorphous alloys based on FeCo can be fabricated by some traditional physical methods such as copper mold casting, rapid quench and single-roller melt spinning [9–11]. To improve the glass forming ability and increase the critical sizes of bulk FeCo-based amorphous alloys, some amorphous-promoting elements such as Si and B should be added in pure metal alloys [12–15]. The chemical method has also been utilized successfully to fabricate the amorphous metal-boron (TM-B, TM = Co, Ni, Fe) powders through chemical reduction of metal ions with KBH_4 in aqueous solution [16]. It has been reported that Fe- or Co-based amorphous alloys can be also fabricated through arc melting by the addition of some rare earth elements such as Tb and Nd [17,18]. Without addition of these glass-formation elements, it is very difficult to fabricate metal-based amorphous alloys due to their poor glass forming ability. However, the additions of these non-magnetic or easily-oxidized glass-formation

elements always introduce contamination and structural instability to the FeCo-based alloys, which would weaken their magnetic performances and the other physical or chemical properties [19].

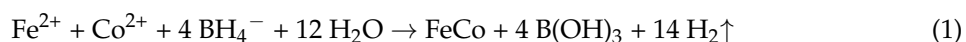
So far, the fabrication of pure amorphous FeCo alloys has been seldom reported because of their weak glass forming ability. In our previous work, we have prepared high-purity amorphous Fe nanoparticles by a chemical method [20]. Our recent work have also revealed that the near-spherical micron-sized FeCo particles with high purity can be fabricated by a direct chemical reduction of Fe²⁺ and Co²⁺ ions with hydrazine hydrate as the reductant in a microemulsion system [21]. Consequently, there is still a challenge to explore an effective route for fabricating pure amorphous FeCo alloys with good stability and enhanced magnetic properties.

As is known, the magnetic and mechanical properties of FeCo alloys are greatly affected by their Fe/Co ratios and microstructure [22]. Our previous study has shown that high magnetization saturation (215 A·m²·kg⁻¹) and low coercivity (73.4 Oe) can be obtained in the chemically synthesized Fe₆₅Co₃₅ micro-sized particles [23]. In this work, we have reported a facile chemical method to fabricate high-purity amorphous Fe₆₅Co₃₅ nanoalloys with slight self-surface modification. The microstructures along with their thermal stability, surface element states and magnetic properties of these amorphous FeCo nanoalloys have been systematically studied.

2. Experimental

2.1. Synthesis of Amorphous FeCo Nanoalloys

The fully amorphous FeCo nanoparticles based on the nominal composition of Fe₆₅Co₃₅ with high purity and controlled morphologies have been fabricated by a directed reduction reaction of Fe²⁺ and Co²⁺ ions with the additions of NaBH₄ as a reducing agent and PVP as surfactant, the schematic formation process for which is shown in Figure 1. A typical procedure is described as follows. Firstly, the suitable amount of FeCl₂·4H₂O (1.2923 g), CoCl₂·6H₂O (0.8323 g) and PVP (1.5 g) were dissolved in distilled water (50 mL) in a three-necked round-bottom flask. Meanwhile, the NaBH₄ (0.7562 g) was dissolved in distilled water (40 mL) in another flask. Then, high-purity N₂ gas was continuously bubbled into the mixed solution containing Co²⁺ and Fe²⁺ ions for 10 min to remove the dissolved oxygen in the mixed liquid. Thirdly, the solution containing NaBH₄ was added dropwise into the three-necked round-bottom flask containing Co²⁺ and Fe²⁺ ions at a rate of 4 mL/min, through a constant-flow pump when stirring vigorously. The reaction process would persist for 50 min and should sustain under high-purity N₂ atmosphere up to the completion of the reaction. The reaction process can be summarized with the following equation:



Finally, the black precipitates were collected by an external magnet after washing them for several times with distilled water and ethanol in sequence and then dried in a vacuum oven at 25 °C for 12 h to get the final products. For further investigation of the effects of different PVP additions on the microstructures for these amorphous FeCo alloys, the other amorphous samples based on the same nominal composition of Fe₆₅Co₃₅ but fabricated without and with PVP additions of 1 and 2 g were also prepared. To investigate crystallization characteristics of these amorphous samples, the as-synthesized sample prepared with 1.5 g PVP additions was annealed under high-purity Ar atmosphere at different temperature from 300 to 550 °C for 10 min.

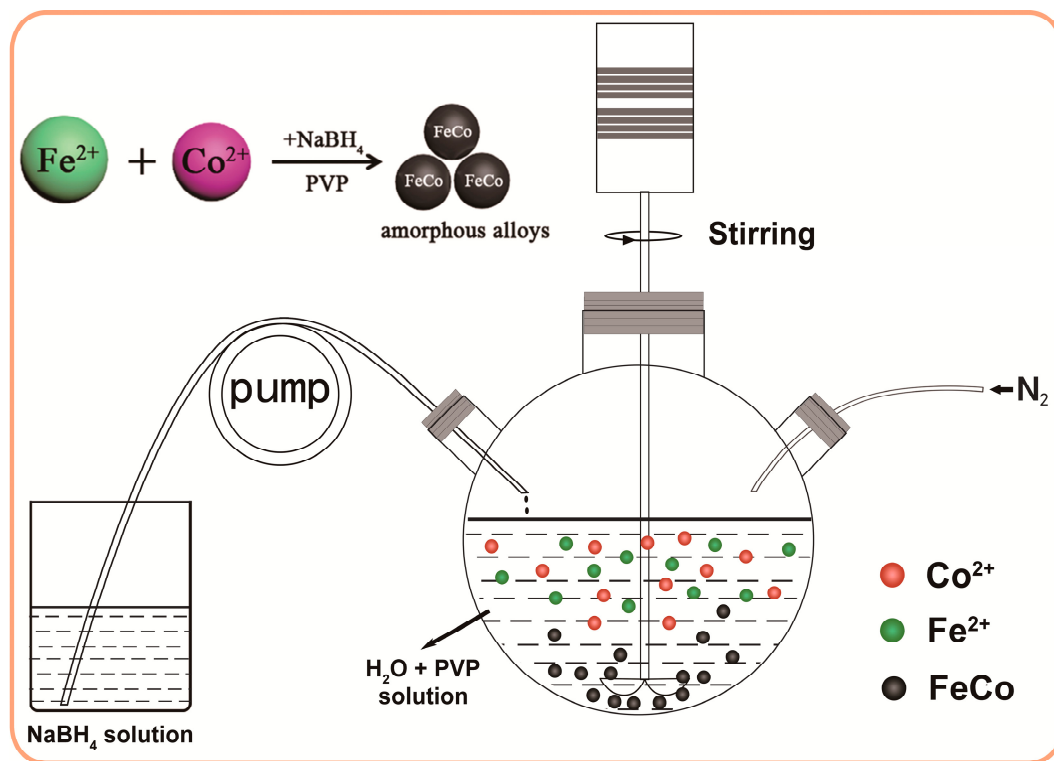


Figure 1. The schematic formation process for the amorphous FeCo nanoalloys.

2.2. Materials Characterization

The phase structures of the samples were characterized by X-ray diffraction (XRD, Rigaku Corporation, Tokyo, Japan) using a D/max 2500PC X-ray diffractometer (Cu $K\alpha$ radiation, $\lambda = 1.5406 \text{ \AA}$). The microstructures of the samples were carried out by a JEOL JEM-2100 transmission electron microscope (TEM, JEOL Co., Ltd., Tokyo, Japan) operated at 200 kV along with a selected-area electron diffraction (SAED). An energy dispersive spectroscope (EDS, JEOL Co., Ltd., Tokyo, Japan) was also used to determine the chemical elements in the products by the same TEM. An inductively coupled plasma optical emission spectroscopy (ICP-OES, Optima 7000 DV, Perkin-Elmer, Waltham, MA, USA) was used to detect the precise compositions of the samples. The thermal properties of these amorphous alloys were analyzed by a differential scanning calorimetry (DSC, STA 449 F3, NETZSCH-Gerätebau GmbH, Selb, Germany) under an Ar atmosphere at a heating rate of $10 \text{ }^\circ\text{C}/\text{min}$. The X-ray photoelectron spectroscopy (XPS, ESCALAB 250Xi, Thermo Fisher Scientific, Waltham, MA, USA) measurement was performed to detect the element states in the samples. The intrinsic magnetic properties of the samples were measured by a vibrating sample magnetometer (VSM, BHV-55, Riken Keiki Co., Ltd., Tokyo, Japan) with a maximum magnetic field of 10 kOe at room temperature. For measuring soft magnetic properties of the products, full-density toroidal samples with an outer diameter of 15 mm, an inner diameter of 9 mm and a sample thickness of 3 mm were produced by directly compacting the products under a static pressure of 1800 MPa. The density of the compacted samples was measured by the Archimedes method. The frequency-dependent magnetic properties for the toroidal samples were measured by an Agilent 4294A precision impedance analyzer (Agilent Technologies, Santa Clara, CA, USA) with a maximum operating frequency of 5 MHz.

3. Results and Discussion

3.1. Structural Analysis

Figure 2 shows the XRD patterns of as-synthesized samples prepared with PVP additions of different amount of 1 g (a), 1.5 g (b), 2 g (c) and without PVP (d) addition. It can be seen that all the three samples prepared with PVP additions exhibit almost the same diffraction characteristics with a broad peak appearing at 2θ of approximately 45° indicating the formation of a fully amorphous phase [24]. The amorphous state of the samples can be further confirmed by their SAED patterns and crystallization characteristics in DSC curves discussed later. However, from the XRD patterns for the sample prepared without PVP addition shown in Figure 2d, four broad peaks can be observed with 2θ values of approximately 34.2° , 44.7° , 59.7° and 82.4° , which can be indexed to FeB and FeCo, respectively. It can be concluded that the PVP additions as the surfactant in the chemical reduction can facilitate the formation of amorphous FeCo alloys. The PVP additions may probably suspend the co-reduction of Fe^{2+} and Co^{2+} ions and restrain their alloying to crystalline FeCo phase so as to promote the formation of amorphous FeCo phase.

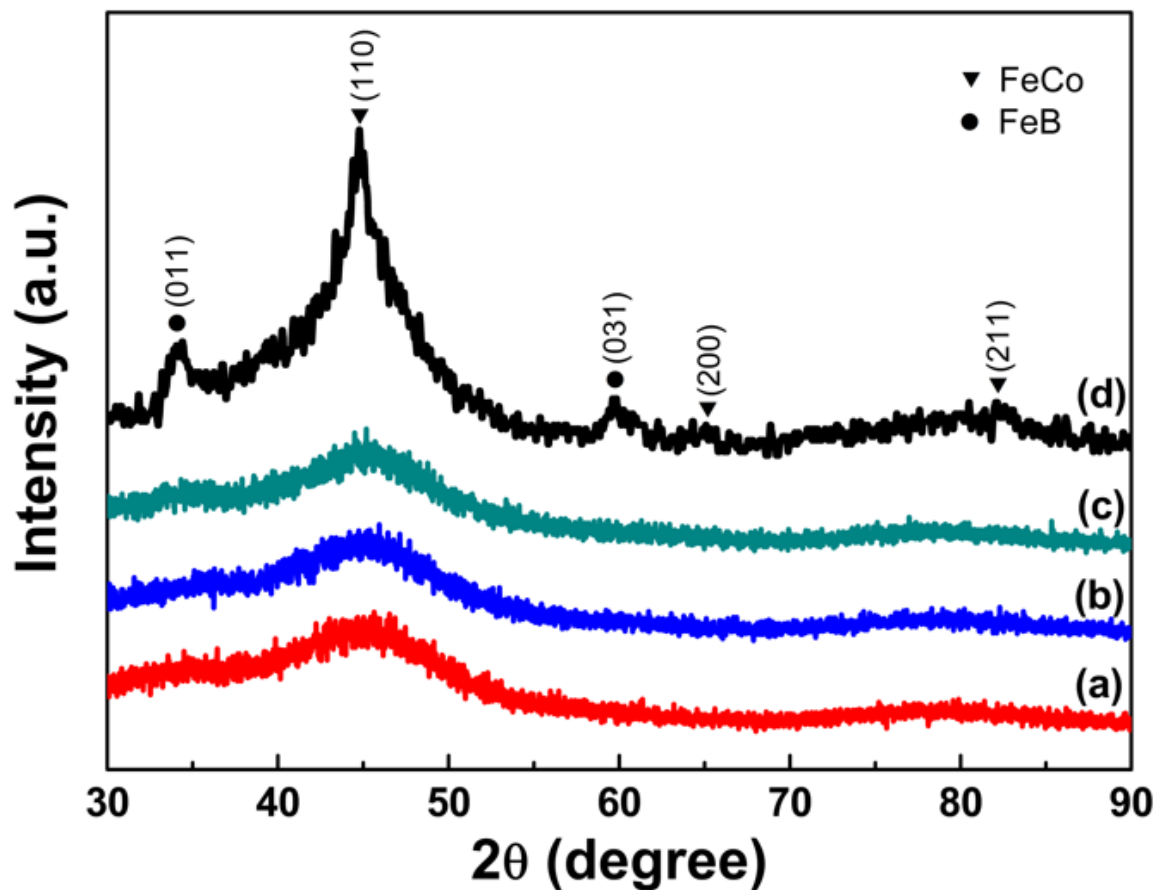


Figure 2. The X-ray diffraction (XRD) patterns of as-synthesized samples prepared with different PVP additions of 1 g (a), 1.5 g (b), 2 g (c) and without PVP (d).

Figure 3 shows the representative TEM micrographs and the SAED patterns along with corresponding histograms for the three amorphous samples prepared with different PVP additions. The number of particles used for the histograms in Figure 3 is approximately 300 for every sample. As shown in Figure 3, the SAED patterns for the three samples only show the diffuse scattering halos indicating the fully amorphous characteristics in these samples. Furthermore, these amorphous

FeCo nanoparticles exhibit a nearly spherical shape with good dispersion. It can be seen the average size can be decreased from 20 to 16 nm for the samples prepared with increasing the PVP additions from 1 to 1.5 g. However, the sample prepared with much more PVP additions of 2 g exhibits much larger average size of 25 nm. The more monodisperse sample with narrow size distribution can be prepared with 1.5 g PVP additions. The actual Fe/Co/O ratios detected by EDS for these amorphous samples are listed in Table 1. Although the small amount of O is detected by EDS measurements, no oxidation can be found in XRD patterns, which indicates that very low surface oxidation occurs in these amorphous nanoparticles. It should be noted that the surface oxidation leads to the shell structure observed in the TEM images for these amorphous FeCo samples, which can be ascribed to the co-effect of the self-surface oxidation and the further oxidation from the preparation process for the TEM samples. It has been reported that the surface oxidation would inevitably occur in high-purity metal-based nanoparticles with small particle size of less than 30 nm and can prevent them from further oxidation in a short period [25]. The surface oxidation is often observed by the TEM but not by the XRD analysis due to their low content within the resolution limit of 5 at. % for the XRD measurement [26,27]. As is known, the TEM observed samples have been often prepared by dispersing the nanoparticles in a pure alcohol or acetone solution, then dropping the dispersed particles on a suitable copper net and finally drying them for TEM observation. Therefore, the preparation process for TEM samples probably increases the surface oxidation for the ultrafine metal nanoparticles due to their easy oxidation. Moreover, the surface oxidation occurring in the nanoparticles can act as the thin area for TEM observation and shows a higher contrast resolution than that for the unoxidized part due to the different structure of the two parts so as to exhibit a seeming shell on the nanoparticles. So a core-shell structure is often observed in TEM images for the ultrafine metal nanoparticles prepared in air. The similar oxide shells can be also observed in the TEM images but not detected by XRD measurement for the ultrafine high-purity Fe [26,28] or CoFe [29] nanoparticles with surface oxidation. The slight self-surface oxidation for amorphous FeCo nanoalloys can be ascribed to the unavoidable surface effects resulting from their small particle sizes and can be also detected by their XPS study discussed below.

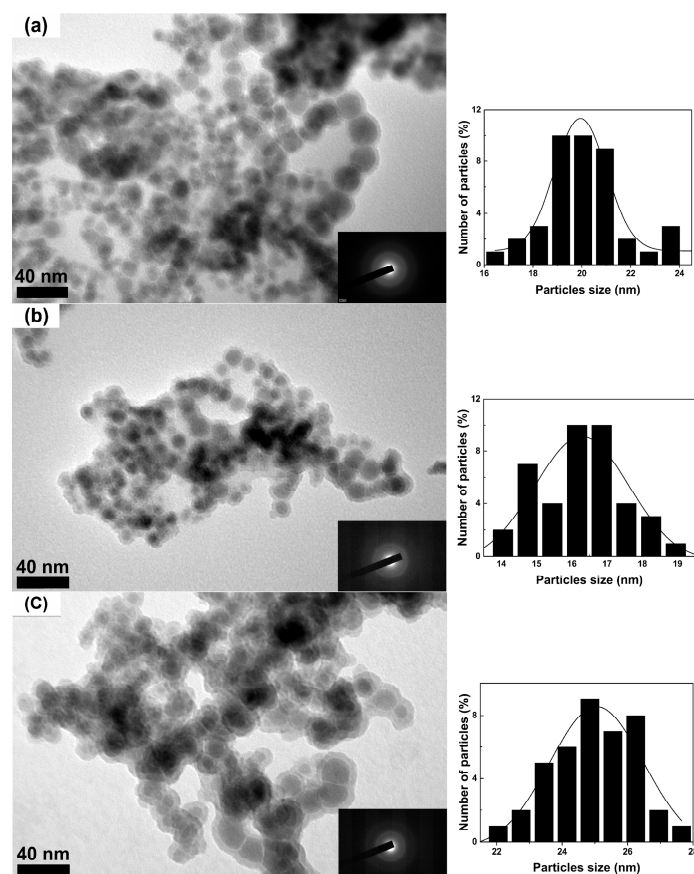


Figure 3. The representative transmission electron microscope (TEM) micrographs and the selected-area electron diffraction (SAED) patterns along with the corresponding histograms on the right side of the figure for amorphous FeCo nanoparticles prepared with different PVP additions of 1 g (a); 1.5 g (b) and 2 g (c).

Table 1. The Fe/Co/O ratios measured by energy dispersive spectroscope (EDS), Fe/Co/B ratios detected by inductively coupled plasma optical emission spectroscopy (ICP-OES), average particle sizes and intrinsic magnetic properties including the values of saturation magnetization M_s and coercivity iH_c of amorphous FeCo nanoparticles prepared with different PVP additions. The saturation magnetization M_s value is defined as the M value corresponding to the maximum magnetic field of 10 KOe in Figure 7 below. The errors of the EDS, ICP-OES and vibrating sample magnetometer (VSM) measurement results are within 2%, 2% and 5%, respectively.

Samples Prepared with Different PVP Addition (g)	The Fe/Co/O Ratio (at. %) Measured by EDS	The Fe/Co/B Ratios (at. %) Detected by ICP-OES	Average Particle Sizes (nm)	M_s (A·m ² /kg)	iH_c (Oe)
(a) 1 g	60.01:32.31:7.68	59.84:31.60:8.56	20	175.0	100.4
(b) 1.5 g	60.78:33.46:5.76	62.77:30.11:7.12	16	196.2	83.3
(d) 2 g	62.12:30.98:6.90	59.67:32.25:7.98	25	182.3	108.5

3.2. Crystallization Characteristics

The DSC measurement was carried out to characterize the crystallization characteristics of the three amorphous samples prepared with different PVP additions. As shown in Figure 4, all the three samples exhibit similar thermal behaviors with a distinct exothermic peak at temperature of approximately 465 °C and another bump at temperature ranging from 316 to 322 °C in the DSC curves, which can be closely related to the two different crystallization process. As is known, the crystallization characteristics of amorphous materials are closely related with their compositions and amorphous phases. From Figure 2 and Table 1, the three amorphous samples exhibit nearly the same amorphous states and also have very similar compositions, which leads to their similar

crystallization characteristics. From Figure 4, the obvious exothermic peak at high temperature is probably associated with the transformation from amorphous FeCo phase to the crystallized FeCo phase, and the exothermic peak at low temperature probably corresponds to another primary crystallization process from a fully amorphous phase to a primary amorphous phase as discussed below. The same crystallization characteristics can be also observed in the other FeCo-based amorphous alloys fabricated by traditional melt-spinning technique [30]. Compared with FeCo-based amorphous alloys with additions of amorphous-promoting elements such as B and Si, the amorphous FeCo nanoparticles exhibit relatively lower transition temperature due to their high-purity [31]. Among three amorphous samples, the sample prepared with 1.5 g PVP additions exhibits the highest transition temperature of 468 °C, which can be ascribed to their uniform particle sizes with narrow size distribution. Another bump-like exothermic peak at low temperature may correspond to the crystallization of primary amorphous phase discussed below.

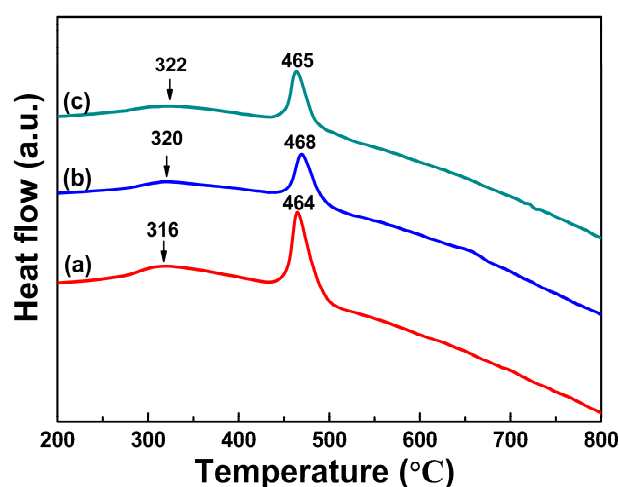


Figure 4. The DSC measurement of amorphous FeCo nanoparticles prepared with different PVP additions of 1 g (a), 1.5 g (b) and 2 g (c).

To further investigate the detailed thermal transition characteristics for these amorphous FeCo nanoalloys, the typical sample prepared with 1.5 g PVP additions has been annealed under Ar gas atmosphere around the exothermic peaks in the DSC curves of 300, 350, 450 and 550 °C for 10 min. Figure 5 shows the XRD patterns of this sample annealed at different temperatures. As shown in Figure 5b,c, the treated samples annealed around low bump-like exothermic peak of 300 and 350 °C still remain fully amorphous states, which confirm the existence of primary amorphous phase in the original amorphous sample. As shown in Figure 5d,e, for the annealed samples treated around high exothermic peak of 450 and 550 °C, three diffraction peaks at 2θ values of 44.8°, 65.1°, and 82.4° corresponding to the crystal planes of (110), (200) and (211) can be observed in their XRD patterns, which are in good agreement with those of bcc-FeCo phase. It has been proved that the crystallized Co nanoparticles with different morphologies often exhibit stable fcc- or hcp-structure [32,33] and their XRD patterns are very different with those for bcc-FeCo phase. Otherwise, the bcc-Co nanoparticles can be obtained as a metastable structure with a strict size limitation of 2–5 nm [34]. Compared with XRD patterns for the original samples and the annealed ones, it can be found that not the other phases containing Co but the single bcc-FeCo phase in fully-annealed amorphous samples can be detected, which confirms the formation of high-purity amorphous FeCo phase but not a mixture of amorphous Co and Fe nanoparticles or amorphous Co@Fe core-shell nanoparticles in the as-synthesized samples prepared with PVP additions. Moreover, the fully-annealed sample treated at a high temperature of 550 °C exhibits a very similar XRD pattern (Figure 5d) with that of the annealed sample treated at 450 °C (Figure 5e) and only a pure bcc-FeCo phase can be observed in these two patterns, which further

confirms the existence of high-purity amorphous FeCo in three as-synthesized amorphous samples. From Figure 5d, the actual transition temperature of the amorphous sample can be also detected to be around 450 °C, which accords well with the results of the above DSC measurement.

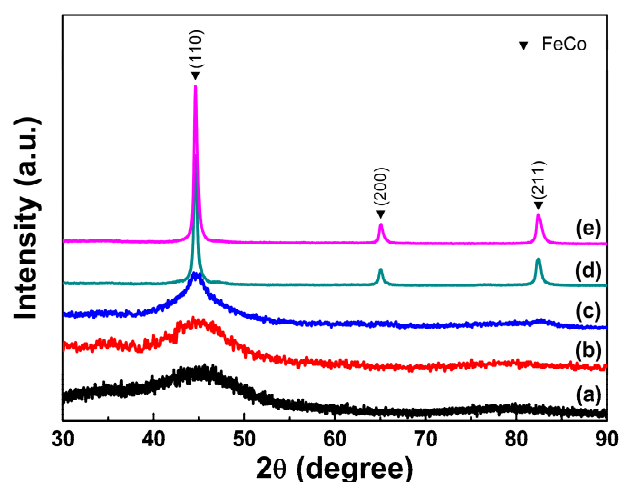


Figure 5. The XRD patterns of the original amorphous FeCo nanoparticles (a) prepared with 1.5 g PVP additions and the treated samples being annealed under Ar gas atmosphere at different temperature of 300 °C (b), 350 °C (c), 450 °C (d) and 550 °C (e) for 10 min.

3.3. X-ray Photoelectron Spectroscopy (XPS) Surface Analysis

The surface element states of Fe, Co, B and O atoms in the as-synthesized amorphous FeCo nanoparticles and another sample prepared without PVP addition have been detected by the XPS narrow-scan spectra shown in Figure 6. The similar surface element states can be observed in the amorphous samples prepared with different PVP addition of 1.5 and 2 g. It can be clearly found from Figure 6A that two Fe 2p peaks with Fe 2p_{3/2} at approximately 706.5 eV and Fe 2p_{1/2} at approximately 719.5 eV are observed for two amorphous samples indicating a pure metallic state of Fe atoms in them [35]. Moreover, the appearance of another two Fe 2p peaks with Fe 2p_{3/2} at approximately 710.0 eV and Fe 2p_{1/2} at approximately 723.3 eV demonstrates the existence of Fe₃O₄ phase in the two amorphous samples [36]. It can be found from Figure 6B that both of the two Co 2p spectra with an appearance of the Co 2p_{3/2} at approximately 778.1 eV and Co 2p_{1/2} at approximately 793.2 eV show a pure metallic Co state in the two amorphous samples [37]. Another two Co 2p peaks with Co 2p_{3/2} at approximately 782.1 eV and Co 2p_{1/2} at approximately 797.1 eV can be observed in Figure 6B indicating the presence of Co₃O₄ and can be further confirmed by their O 1s spectra with the peak around 530.7 eV shown in Figure 6C [38]. As shown in Figure 6D, the B 1s spectra for two amorphous samples also exhibit very similar curves and peak locations, which indicate the same B element state. The B 1s peaks at 192.1 and 187.9 eV can be attributed to the existence of FeB or CoB phases on surface of the amorphous samples [39,40]. The slight shift of peak location of 0.6 eV in XPS narrow-scan spectra for the two amorphous samples can be ascribed to of their different surface compositions, which are verified by the EDS investigation in Table 1. However, the Fe 2p spectra for the sample without PVP addition exhibit two Fe 2p peaks with Fe 2p_{3/2} at approximately 710.8 eV and Fe 2p_{1/2} at approximately 724.2 eV indicating the existence of Fe₃O₄ phase and while the appearance of two Co 2p peaks with Co 2p_{3/2} at 780.6 eV and Co 2p_{1/2} at 796.6 eV along with a broad bump at approximately 786.1 eV, which accords with those of CoFe₂O₄ phase [41]. Thus, no pure metallic Co but very weak pure metallic Fe state detected for the sample prepared without PVP addition indicates their more serious surface oxidation. It can be found that the PVP additions during the preparation can not only promote the formation of amorphous FeCo nanoparticles, but also weaken their surface oxidation.

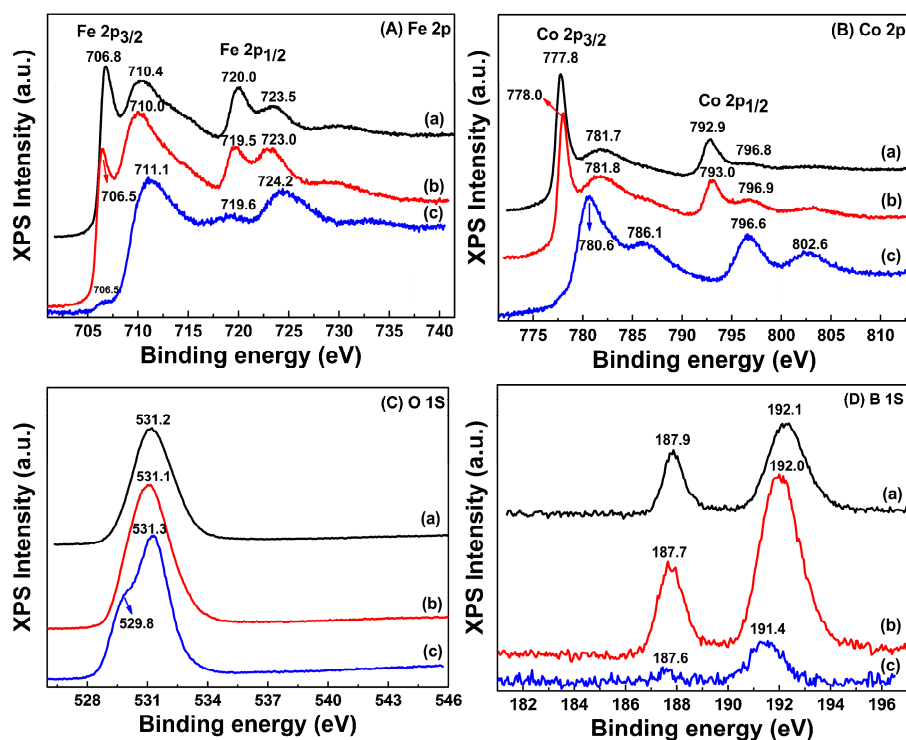


Figure 6. The XPS narrow-scan spectra of Fe 2p (A), Co 2p (B), O 1s (C) and B 1s (D) for amorphous FeCo nanoalloys prepared with different PVP additions of 1.5 g (a), 2 g (b) and the sample prepared without PVP (c).

As is known, the XPS investigation provides the surface element information of the samples for the photoelectron probing depth is within only a few angstroms. As discussed above, weak O and B concentration for amorphous FeCo nanoparticles is observed by XPS measurement. However, no oxidation or B-contained phases are detected by the XRD measurement for the original amorphous samples and the fully annealed ones. To make sure the precise compositions for these amorphous particles, the ICP-OES has been adopted to detect the elements in the samples. As shown in Table 1, besides Fe and Co elements, another B element is detected by ICP-OES, which however cannot be detected by EDS due to the low surface B concentration outside the measuring accuracy of EDS. Combined with the XPS, ICP-OES and XRD results, it can be deduced reasonably that self-surface modification including weak surface oxidation and low surface B concentration occurs in these chemically-synthesized amorphous FeCo nanoparticles. It has been reported that air stability for the chemically-synthesized Co nanoparticles with size range of 3–11 nm can be greatly improved by their gentle surface oxidation [42]. In this work, the as-synthesized products have been preserved without protective atmosphere after completion of their preparation and measured within a week. So the weak surface oxidation occurring in these amorphous FeCo nanoparticles can probably delay their further oxidation in air within a short period, for no oxidation can be detected by their XRD measurements. Furthermore, the low surface B aggregation can also protect these amorphous FeCo nanoparticles from further oxidation and lead to their good air and thermal stability [20]. From the above discussion, it can be concluded that the suitable PVP additions promote the formation of high-purity amorphous FeCo nanoalloys with slight self-surface modification. Furthermore, the different PVP amounts show an obvious influences on the particle sizes with their distribution and the Fe/Co ratios for these amorphous samples, and also protect the amorphous FeCo nanoalloys from further oxidation.

3.4. Magnetic Properties

Figure 7 shows the room-temperature hysteresis loops for the three amorphous FeCo samples. It can be found that all the three samples exhibit typical ferromagnetism with good intrinsic magnetic properties. The values of saturation magnetization M_s and coercivity iH_c of the three samples are also listed in Table 1. The high M_s values of 175.0, 196.2 and 182.3 $\text{A}\cdot\text{m}^2\cdot\text{kg}^{-1}$ are obtained for the samples prepared with PVP additions of 1, 1.5 and 2 g, respectively. Compared with the M_s value ($215 \text{ A}\cdot\text{m}^2\cdot\text{kg}^{-1}$) of crystalline $\text{Fe}_{65}\text{Co}_{35}$ micro-sized particles, the slight decreasing of M_s for the amorphous FeCo nanoparticles can be ascribed to their surface oxidation along with surface B concentration and the spin canting effect for nanoparticles [43,44]. The product prepared with 1.5 g PVP additions exhibits highest M_s value of $196.2 \text{ A}\cdot\text{m}^2\cdot\text{kg}^{-1}$ among the three samples due to the low surface O and B content as shown in Table 1. It can be also found from Table 1 that these amorphous samples exhibit relatively high coercivity of 83.3–108.5 Oe by virtue of their smaller particle sizes and surface oxidation. The amorphous FeCo nanoparticles prepared with 1.5 g PVP addition also exhibit lowest iH_c value of 83.3 Oe due to their narrow size distribution.

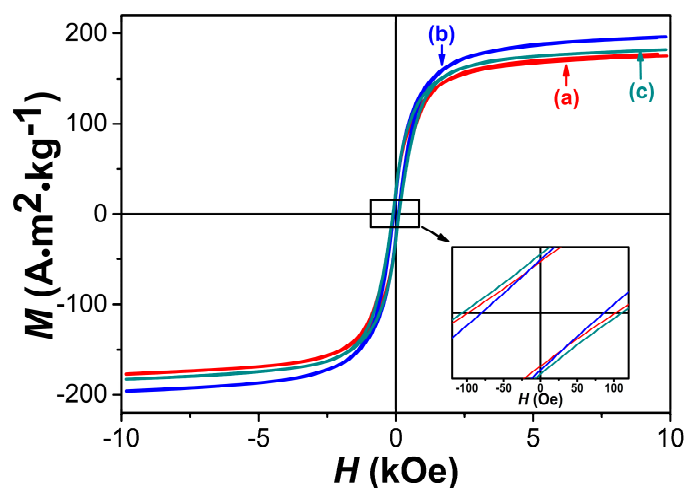


Figure 7. Magnetic hysteresis loops of amorphous FeCo nanoparticles prepared with different PVP additions of 1 g (a), 1.5 g (b) and 2 g (c).

For investigating soft magnetic properties of the as-synthesized amorphous FeCo product, a full-density toroidal sample (shown in the inset of Figure 8) has been produced by directly compacting the amorphous product prepared with 1.5 additions under a static pressure of approximately 1800 MPa. Another toroidal crystalline FeCo sample with the same thickness of 3 mm has also been fabricated by compacting high-purity $\text{Fe}_{65}\text{Co}_{35}$ particles with an average size of approximately $120 \mu\text{m}$ (Commercial products, purchased from Titd Metal materials Co., Ltd., Changsha, China) under the same pressure. The fully compacted amorphous FeCo sample exhibits a high density of $7.20 \text{ g}/\text{cm}^3$ due to its high purity, but comparatively lower than that of the compressed micron-sized $\text{Fe}_{65}\text{Co}_{35}$ particles under the same pressure ($7.62 \text{ g}/\text{cm}^3$), which can be ascribed to the strong aggregation forces occurring in the compressed nanoparticles [45]. Figure 8 shows frequency-dependent complex permeability (the real part μ' and imaginary part μ'') measured at frequencies from 40 Hz to 5 MHz for the two toroidal samples. Although the permeability and core loss of a toroidal core strongly depend on its thickness, in this work, the different influences of thickness on the permeability and core loss of the two samples can be ignored due to their same thickness. The complex permeability properties of these two toroidal cores with the same thickness can be investigated to effectively compare their closed-loop magnetic properties. From Figure 8, the amorphous FeCo product exhibits slightly lower μ' values than those of crystalline FeCo sample at frequencies below 1.5 MHz, but higher μ' values at frequencies from 1.5 to 5 MHz, which indicates that the amorphous sample possesses

a better ac permeability. The lower μ' values at low frequencies for amorphous sample can be ascribed to its relatively low M_s value, high iH_c value and lower density resulting from its weak surface oxidation and low surface B aggregation [2]. Furthermore, the variation of μ' values with increasing frequency for amorphous FeCo product shows a gradual descending trend and very low μ'' values at operating frequencies up to 5 MHz are also observed, indicating lower core loss in the amorphous FeCo product, which can be ascribed to its much higher electrical resistivity (approximately $1.2\text{--}2.4 \times 10^{-4} \Omega\cdot\text{cm}$) [46,47] than that of high-purity FeCo ($1\text{--}10 \times 10^{-6} \Omega\cdot\text{cm}$) [48]. Nevertheless, the amorphous FeCo sample exhibits better frequency-dependent magnetic characteristics with comprehensive high μ' and low μ'' values at operating frequencies up to 5 MHz. From the above discussion, it can be concluded that these amorphous FeCo products possess high stability, good intrinsic and frequency-dependent magnetic characteristics, and show their significant potential applications in high-power magnetic devices.

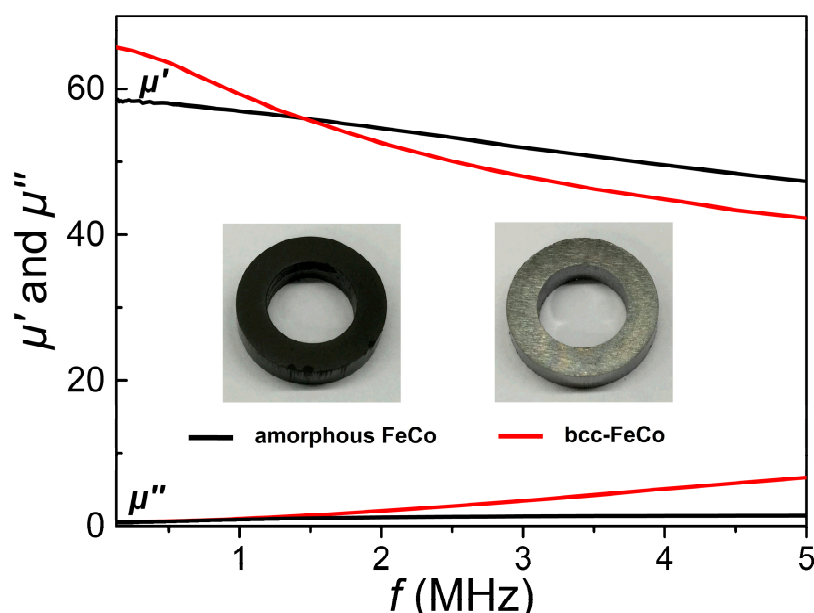


Figure 8. The complex permeability spectra for the two compacted samples of the amorphous FeCo prepared with 1.5 g PVP additions and high-purity Fe₆₅Co₃₅ particles.

4. Conclusions

The fully amorphous FeCo nanoalloys with low surface modification have been synthesized by a direct chemical reduction reaction of both Fe²⁺ and Co²⁺ ions with NaBH₄ as the reductant along with PVP as the surfactant. The PVP additions have been proved to promote the formation of amorphous FeCo phase with high purity. The suitable PVP additions of 1.5 g can lead to the formation of uniform amorphous FeCo nanoparticles with a narrow size distribution and low surface oxygen content, which result in their high saturation magnetization of 196.2 A·m²·kg⁻¹ and low coercivity of 83.3 Oe. The chemically synthesized FeCo nanoparticles exhibit high transition temperatures of 464–468 °C, which can be ascribed to their low surface B concentration. The full-density amorphous FeCo toroidal sample with a high density of 7.20 g/cm³ can be obtained by directly compacting the as-synthesized amorphous FeCo nanoalloys under a static pressure of 1800 MPa. Good frequency-dependent magnetic characteristics are also achieved in the fully compacted amorphous FeCo sample. The chemical synthesis for amorphous FeCo nanoalloys in this work may also provide a new insight for fabrication of metallic glasses or amorphous alloys.

Acknowledgments: This work was supported by Beijing Natural Science Foundation under Grant No. 2132039 and the National Natural Science Foundation of China under Grant No. 51101007.

Author Contributions: Bai Yang planned and directed the experiments. Yue Wu prepared the samples and performed the XRD, XPS and TEM measurements. Xiaopan Li measured magnetic properties of the samples. Ronghai Yu helped to analyze the results. Bai Yang and Yue Wu wrote the paper, which was refined by Bai Yang and reviewed by all the authors.

Conflicts of Interest: The authors declare no conflict of interest.

References

1. Kolhatkar, A.G.; Nekrashevich, I.; Litvinov, D.; Willson, R.C.; Lee, T.R. Cubic silica-coated and amine-functionalized FeCo nanoparticles with high saturation magnetization. *Chem. Mater.* **2013**, *25*, 1092–1097.
2. Yang, B.; Li, X.P.; Guo, R.Y.; Yu, R.H. Oxidation fabrication and enhanced soft magnetic properties for core-shell FeCo/CoFe₂O₄ micron-nano composites. *Mater. Des.* **2017**, *121*, 272–279.
3. Meffre, A.; Mehdaoui, B.; Connord, V.; Carrey, J.; Fazzini, P.F.; Lachaize, S.; Respaud, M.; Chaudret, B. Complex nano-objects displaying both magnetic and catalytic properties: A proof of concept for magnetically induced heterogeneous catalysis. *Nano Lett.* **2015**, *15*, 3241–3248.
4. Martel, S. Magnetic nanoparticles in medical nanorobotics. *J. Nanopart. Res.* **2015**, *17*, 75–89.
5. Bhattacharya, S.; Lass, E.A.; Poon, S.J.; Shiflet, G.J.; Rawlings, M.; Daniil, M.; Willard, M.A. Magnetic properties and thermal stability of (Fe,Co)-Mo-B-P-Si metallic glasses. *J. Appl. Phys.* **2012**, *111*.
6. Torrens-Serra, J.; Bruna, P.; Stoica, M.; Roth, S.; Eckert, J. Glass forming ability, thermal stability, crystallization and magnetic properties of [(Fe,Co,Ni)_{0.75}Si_{0.05}B_{0.20}]₉₅Nb₄Zr₁ metallic glasses. *J. Non-Cryst. Solids* **2013**, *367*, 30–36.
7. Liu, L.; Zhu, J.B.; Hou, C.; Li, J.C.; Jiang, Q. Dense and smooth amorphous films of multicomponent FeCoNiCuVZrAl high-entropy alloy deposited by direct current magnetron sputtering. *Mater. Des.* **2013**, *46*, 675–679.
8. Han, Y.M.; Wang, Z.; Che, X.H.; Chen, X.G.; Li, W.R.; Li, Y.L. Influence of Co content on the structure and magnetic permeability of nanocrystalline (Fe_{1-x}Co_x)_{73.5}Cu₁Nb₃Si_{13.5}B₉ alloys. *Mater. Sci. Eng. B* **2009**, *156*, 57–61.
9. Inoue, A.; Shen, B.L.; Chang, C.T. Super-high strength of over 4000 MPa for Fe-based bulk glassy alloys in [(Fe_{1-x}Co_x)_{0.75}B_{0.2}Si_{0.05}]₉₆Nb₄ system. *Acta Mater.* **2004**, *52*, 4093–4099.
10. Han, M.; Qin, J.; Deng, L. Microwave permeability of nanocrystalline alloys (Fe_{0.67}Co_{0.33})₇₈Nb₆B₁₅Cu₁ and (Fe_{0.67}Co_{0.33})₇₈Nb₆Al₆B₉Cu₁. *J. Alloys Compd.* **2012**, *543*, 79–83.
11. Han, Y.; Wang, Z. Excellent high-temperature magnetic softness in a wide temperature for FeCo-based nanocrystalline alloy. *J. Non-Cryst. Solids* **2016**, *434*, 92–95.
12. Platt, C.L.; Minor, M.K.; Klemmer, T.J. Magnetic and structural properties of FeCoB thin films. *IEEE Trans. Magn.* **2001**, *7*, 2302–2304.
13. Ogawa, H.; Miura, H. Compositional dependence of amorphization of M–C–Si (M=Fe, Co or Ni) materials by mechanical alloying. *J. Mater. Process. Technol.* **2003**, *143*, 256–260.
14. Guo, W.; Zhang, J.; Wu, Y.; Hong, S.; Qin, Y. Fabrication and characterization of Fe-based amorphous coatings prepared by high-velocity arc spraying. *Mater. Des.* **2015**, *78*, 118–124.
15. Li, X.; Chen, J.; Zhang, K. High temperature deformation behavior of amorphous Fe₇₈Si₉B₁₃/nano-Ni laminated composite. *Mater. Des.* **2009**, *30*, 2665–2669.
16. Corrias, A.; Ennas, G.; Musinu, A.; Marongiu, G.; Paschina, G. Amorphous transition metal-boron ultrafine particles prepared by chemical methods. *Chem. Mater.* **1993**, *5*, 1722–1726.
17. Li, F.S.; Zhang, T.; Inoue, A.; Guan, S.K.; Shen, N.F. (Fe,Co)–Zr–Nd–B bulk amorphous alloys with good soft magnetic properties. *Intermetallics* **2004**, *12*, 1139–1142.
18. Jian, H.; Luo, W.; Tao, S.; Yan, M. Mechanical and magnetic properties of (Fe₇₂Mo₄B₂₄)_{100-x}Tb_x, (x = 4, 5, 6, 7 at. %) bulk glassy alloys. *J. Alloys Compd.* **2010**, *505*, 315–318.
19. Taghvaei, A.H.; Bednarčik, J.; Eckert, J. Atomic structure and thermal behavior of (Co_{0.65}Fe_{0.35})₇₂Ta₈B₂₀ metallic glass with excellent soft magnetic properties. *Intermetallics* **2016**, *69*, 21–27.
20. Yang, B.; Yang, X.Y.; Li, X.P.; Cao, Y.; Yu, R.H. Surface modification and enhanced performance of chemically synthesized nanosized amorphous Fe particles. *J. Supercond. Nov. Magn.* **2015**, *28*, 2177–2182.
21. Yang, B.; Cao, Y.; Zhang, L.; Li, R.F.; Yang, X.Y.; Yu, R.H. Controlled chemical synthesis and enhanced performance of micron-sized FeCo particles. *J. Alloys Compd.* **2014**, *615*, 322–326.

22. Klencsár, Z.; Németh, P.; Sándor, Z.; Horváth, T.; Sajó, I.E.; Mészáros, S.; Mantilla, J.; Coaquira, J.A.H.; Garg, V.K.; Kuzmann, E.; et al. Structure and magnetism of Fe–Co alloy nanoparticles. *J. Alloys Compd.* **2016**, *674*, 153–161.
23. Li, X.P.; Yang, B.; Yang, X.Y.; Cao, Y.; Yu, R.H. Structural formation and improved performances of chemically synthesized composition-controlled micron-sized Fe_{100-x}Co_x particles. *J. Supercond. Nov. Magn.* **2016**, *29*, 417–422.
24. Liaw, B.J.; Chiang, S.J.; Tsai, C.H.; Chen, Y.Z. Preparation and catalysis of polymer-stabilized NiB catalysts on hydrogenation of carbonyl and olefinic groups. *Appl. Catal. A Gen.* **2005**, *284*, 239–246.
25. Fuller, R.O.; Goh, B.M.; Koutsantonis, G.A.; Loedolff, M.J.; Saunders, M.; Woodward, R.C. A simple procedure for the production of large ferromagnetic cobalt nanoparticles. *Dalton Trans.* **2016**, *45*, 11983–11989.
26. Joseyphus, R.J.; Shinoda, K.; Kodama, D.; Jeyadevan, B. Size controlled Fe nanoparticles through polyol process and their magnetic properties. *Mater. Chem. Phys.* **2010**, *123*, 487–493.
27. Arun, T.; Prakash, K.; Joseyphus, R.J. Synthesis and magnetic properties of Prussian blue modified Fe nanoparticles. *J. Magn. Mater.* **2013**, *345*, 100–105.
28. Zhang, S.; Jiang, G.M.; Filsinger, G.T.; Wu, L.H.; Zhu, H.Y.; Lee, J.H.; Wu, Z.B.; Sun, S.H. Halide ion-mediated growth of single crystalline Fe nanoparticles. *Nanoscale* **2014**, *6*, 4852–4856.
29. Wang, C.; Peng, S.; Lacroix, L.M.; Sun, S.H. Synthesis of high magnetic moment CoFe nanoparticles via interfacial diffusion in core/shell structured Co/Fe nanoparticles. *Nano Res.* **2009**, *2*, 380–385.
30. Zheng, Z.; Zhao, G.; Xu, L.; Wang, L.; Yan, B. Influence of Ni addition on nanocrystallization kinetics of FeCo-based amorphous alloys. *J. Non-Cryst. Solids* **2016**, *434*, 23–27.
31. Kai, W.; Wu, Y.H.; Chen, W.S.; Tsay, L.W.; Jia, H.L.; Liaw, P.K. Air-oxidation behavior of a [(Fe₅₀Co₅₀)₇₅B₂₀Si₅]₉₆Nb₄ bulk metallic glass at 500–650 °C. *Corros. Sci.* **2013**, *66*, 26–32.
32. Song, Y.J.; Modrow, H.; Henry, L.L.; Saw, C.K.; Doomes, E.E.; Palshin, V.; Hormes, J.; Kumar, C.S.S.R. Microfluidic synthesis of cobalt nanoparticles. *Chem. Mater.* **2006**, *18*, 2817–2827.
33. Zhang, Z.D.; Wang, H.M.; Qin, C.; Chen, S.H.; Ji, X.J.; Sun, K.; Chen, M.; Fan, R.H.; Han, X. Fabrication and magnetic properties of electrospun cobalt nanofibers. *Mater. Des.* **2016**, *89*, 543–548.
34. Ram, S. Allotropic phase transformations in HCP, FCC and BCC metastable structures in Co-nanoparticles. *Mater. Sci. Eng. A* **2001**, *304*, 923–927.
35. Yang, X.Y.; Yang, B.; Li, X.P.; Cao, Y.; Yu, R.H. Structural-controlled chemical synthesis of nanosized amorphous Fe particles and their improved performances. *J. Alloys Compd.* **2015**, *651*, 551–556.
36. Yamashita, T.; Hayes, P. Analysis of XPS spectra of Fe²⁺ and Fe³⁺ ions in oxide materials. *Appl. Surf. Sci.* **2008**, *254*, 2441–2449.
37. Sheu, H.H.; Lu, C.E.; Lee, H.B.; Pu, N.W.; Wu, P.F.; Hsieh, S.H.; Ger, M.D. Electrodeposition of black chromium-cobalt alloy based on trivalent sulfate electrolyte. *J. Taiwan Inst. Chem. Eng.* **2015**, *59*, 496–505.
38. Li, J.; Lu, G.; Wu, G.; Mao, D.; Guo, Y.; Wang, Y.; Guo, Y. Effect of TiO₂ crystal structure on the catalytic performance of Co₃O₄/TiO₂ catalyst for low-temperature CO oxidation. *Catal. Sci. Technol.* **2014**, *4*, 1268–1275.
39. Shen, W.; Mu, Y.; Xiao, T.; Ai, Z. Magnetic Fe₃O₄-FeB nanocomposites with promoted Cr (VI) removal performance. *Chem. Eng. J.* **2016**, *285*, 57–68.
40. Shen, X.C.; Dai, M.; Gao, M.; Zhao, B.; Ding, W. Solvent effects in the synthesis of CoB catalysts on hydrogen generation from hydrolysis of sodium borohydride. *Chin. J. Catal.* **2013**, *34*, 979–985.
41. Meng, Y.D.; Chen, D.R.; Jiao, X.L. Synthesis and characterization of CoFe₂O₄ hollow spheres. *Eur. J. Inorg. Chem.* **2008**, *25*, 4019–4023.
42. Lu, A.H.; Salabas, E.L.; Schüth, F. Magnetic nanoparticles: Synthesis, protection, functionalization, and application. *Angew. Chem. Int. Ed.* **2007**, *46*, 1222–1244.
43. Ahmed, J.; Kumar, B.; Mugweru, A.M.; Trinh, P.; Ramanujachary, K.V.; Lofland, S.E.; Ganguli, A.K. Binary Fe–Co alloy nanoparticles showing significant enhancement in electrocatalytic activity compared with bulk alloys. *J. Phys. Chem. C* **2010**, *114*, 18779–18784.
44. Kim, B.H.; Lee, N.; Kim, H.; An, K.; Park, Y.I.; Choi, Y.; Shin, K.; Lee, Y.; Kwon, S.G.; Na, H.B.; et al. Large-scale synthesis of uniform and extremely small-sized iron oxide nanoparticles for high-resolution T₁ magnetic resonance imaging contrast agents. *J. Am. Chem. Soc.* **2011**, *133*, 12624–12631.
45. Costa, T.M.H.; Gallas, M.R.; Benvenuti, E.V.; Da-Jornada, J.A.H. Study of nanocrystalline γ -Al₂O₃ produced by high-pressure compaction. *J. Phys. Chem. B* **1999**, *103*, 4278–4284.

46. Inoue, A.; Takeuchi, A.; Shen, B.L. Formation and functional properties of Fe-based bulk glassy alloys. *Mater. Trans.* **2001**, *42*, 970–978.
47. Inoue, A.; Zhang, T.; Koshiba, H.; Makino, A. New bulk amorphous Fe–(Co,Ni)–M–B (M = Zr, Hf, Nb, Ta, Mo, W) alloys with good soft magnetic properties. *J. Appl. Phys.* **1998**, *83*, 6326–6328.
48. Redjdal, N.; Salah, H.; Hauet, T.; Menari, H.; Chérif, S.M.; Gabouze, N.; Azzaz, M. Microstructural, electrical and magnetic properties of Fe₃₅Co₆₅ thin films grown by thermal evaporation from mechanically alloyed powders. *Thin Solid Films* **2014**, *552*, 164–169.



© 2018 by the authors. Licensee MDPI, Basel, Switzerland. This article is an open access article distributed under the terms and conditions of the Creative Commons Attribution (CC BY) license (<http://creativecommons.org/licenses/by/4.0/>).